

# **Design Principles for Tailoring Heat Transport via Iris-Gated Core–Double–Shell Nanoparticles in the Context of Photothermal Therapies**

*Javier González-Colsa\*, Fernando Bresme, Pablo Albella\**

J. González-Colsa, P. Albella

Group of Optics, Department of Applied Physics, University of Cantabria, 39005 Santander, Spain.

E-mail: [javier.gonzalezcols@unican.es](mailto:javier.gonzalezcols@unican.es), [pablo.albella@unican.es](mailto:pablo.albella@unican.es).

F. Bresme

Department of Chemistry, Molecular Sciences Research Hub, Imperial College London, London W12 0BZ, UK.

**Funding:** This work was financed by the Spanish Ministerio de Ciencia e Innovación under project MOPHOSYS (grant no. PID2022-139560NB-I00).

**Keywords:** Thermoplasmonics, Core–shell nanoparticles, Thermal asymmetry, Heat transport, Photothermal applications, Nanostructures

## Abstract

The rational design of Janus nanostructures that combine efficient optical absorption with controlled thermal transport is essential for advancing plasmonic photothermal therapies and related applications. Here, we introduce a theoretical and computational framework to investigate core–double–shell nanoparticles and their asymmetric version, the iris-gated core–double–shell architecture. The optical response of the structures is first evaluated using generalized Mie theory and subsequently validated through FEM and FDTD simulations, ensuring a consistent description of their electromagnetic and thermal behavior. To systematically map the space of variables, we defined a multi-objective figure of merit that integrates absorption efficiency, absorption cross section, and polymer-layer thickness. Furthermore, we define a thermal gain parameter that quantifies energy densification and complements the analysis of thermal directionality. Our results reveal a near-optimal configuration with parameters  $(r_c, \delta_{Au}, \delta_p, \theta) = (36 \text{ nm}, 5 \text{ nm}, 40 \text{ nm}, 70^\circ)$ , capable of producing a temperature rise of 20–23 °C, with 67% of the thermal flux directed toward the upper hemispace and yielding a 50% focusing enhancement relative to the symmetric case. This design preserves geometric simplicity and high symmetry while delivering robust thermal asymmetry, thereby facilitating experimental implementation. Beyond photothermal therapies, the proposed methodology constitutes a versatile platform for the rapid screening and optimization of layered nanostructures, adaptable to diverse materials, excitation wavelengths, and functional objectives in nanophotonics.

## 1. Introduction

Thermoplasmonics has established itself as a versatile platform for generating highly localized temperature increases by exploiting the strong light–matter interaction supported by plasmonic nanostructures<sup>[1]</sup>. When metallic nanoparticles are excited at their Localized Surface Plasmon Resonances (LSPRs), incident electromagnetic energy is efficiently converted into heat through resistive dissipation<sup>[2,3]</sup>. A key strength of this mechanism lies in its high degree of tunability, both the spectral position and magnitude of the plasmonic resonance can be engineered by adjusting particle size, morphology, and composition<sup>[4]</sup>. This tunability has enabled novel applications across nanoscience ranging from photocatalysis and solar energy harvesting to imaging and nanomedicine, among others<sup>[5]</sup>.

In this work, we focus specially on PhotoThermal Therapy (PTT), an application in which thermoplasmonic performance is governed by stringent biological and technological constraints. The primary goal of PTT is the selective ablation of malignant cells via highly localized heating, ideally achieving single cell or even sub cellular resolution. For this purpose, plasmonic tunability is essential. Absorption must be engineered within the biological transparency windows (NIR I-II), where optical attenuation is reduced<sup>[6]</sup>. Under such conditions, water can reasonably be taken as the surrounding medium and biocompatible dielectric materials are typically employed for structural components. This modelling approach, widely adopted in theoretical/numerical studies of plasmonic nanoparticles for PTT<sup>[7–10]</sup>, provides an adequate description of optical and thermal behavior while maintaining computational simplicity required for efficient numerical modeling.

A central challenge in PTT is related to spatial specificity<sup>[11]</sup>. Although biochemical functionalization governs biological targeting, most homogeneous nanostructures, even those with anisotropic shapes, yield nearly isotropic temperature fields under illumination<sup>[1,2,8]</sup>. This isotropy can lead to off-target heating and potential damage to the surrounding healthy tissue. To overcome this limitation, hybrid architectures such as Janus particles or composite nanoparticles have been explored. Their material heterogeneity enables the combination of distinct functionalities (chemical, optical, or catalytic) within a single colloid<sup>[12]</sup>. Such hybrid platforms have been successfully employed in drug delivery, biosensing, and catalysis<sup>[13]</sup>, where multifunctionality provides a clear advantage.

In the context of thermoplasmonics, material heterogeneity introduces an additional degree of freedom: by appropriately combining plasmonic components with materials of contrasting thermal conductivities (high and low), it becomes possible to generate asymmetric temperature profiles under both continuous and pulsed excitation<sup>[14–16]</sup>. Compared to fully symmetric counterparts, such designs can preferentially redistribute heat toward specific spatial regions, enabling directional thermal flux and energy focusing. Nevertheless, the total heat generated by an individual nanoparticle remains limited by its volume, often requiring dense colloidal suspensions for effective therapy. This requirement imposes tight constraints on synthetic reproducibility and monodispersity, particularly for complex Janus-type geometries, thereby motivating the search for simpler architectures capable of producing robust thermal asymmetry.

Here, we propose a minimal yet effective strategy to address this challenge: an Iris-gated Core–Double–Shell (ICDS) nanoparticle. We begin with a highly symmetric stratified sphere, consisting of a glass core to redshift the plasmon resonance into the first biological window (NIR-I), a gold shell serving as the primary heat source, and a polymer overshell acting as thermal insulator. Then, we incorporate a single, controlled and as small as possible geometric perturbation: a conical iris aperture in the polymer overshell. This minimal symmetry breaking enables both directional thermal transport and enhanced thermal focusing while preserving fabrication simplicity. To explore the space of geometrical parameters efficiently, we developed a computational optimization framework based on a multi-objective figure of merit that drastically reduces the initial search domain. Our analysis reveals that ICDS nanoparticles can simultaneously maximize temperature rise, directional heat flux, and local energy densification, all while preserving high structural symmetry and fabrication feasibility. Beyond its immediate implications for PTT, the approach provides a generalizable methodology for the rapid screening of layered nanostructures across different material combinations and excitation wavelengths, thereby establishing a flexible design principle for the broader nanophotonics community.

## 2. Methods

Given the theoretical-computational nature of this study, we employed a combination of analytical electrodynamics, full-wave numerical solvers, and finite-element thermal modeling. Specifically, optical simulations were conducted using generalized Mie theory, Finite-Difference Time-Domain (FDTD, Ansys Lumerical), and Finite Element Method (FEM,

Comsol Multiphysics). All analytical calculations were carried out with freely available software packages.

## 2.1 Optical Modeling of Core-Double-Shell Nanoparticles

To characterize the optical response of the symmetric precursor core–double–shell (CDS) nanoparticles, we used the generalized Mie theory, which provides an exact analytical solution for stratified spherical particles. The implementation adopted here, corresponds to the *MatScat* package developed by Jan Schäfer (*MatScat*), freely available through the MATLAB Central File Exchange<sup>[17]</sup>. Within this framework, the refractive indices were set as follows:  $n = 1.33$  for water (surrounding medium),  $n = 1.41$  for the polymer overshell (corresponding to PDMS), and  $n = 1.51$  for the glass core. The optical constants of gold were taken from Johnson & Christie data set<sup>[18]</sup>, accessible via the *RefractiveIndex.INFO* database.

The Mie formalism requires a truncation threshold for the multipolar series expansion of the scattering coefficients, controlled by the convergence parameter, *conv*, in the expression<sup>[17]</sup>:

$$M = \text{ceil}(\text{conv} * (x + 4 * (x^{(1/3)}) + 2));$$

where the size parameter is  $x = 2\pi a/\lambda$ , with  $a$  the particle radius and  $\lambda$  the incident wavelength. Since the systems under study lie in the subwavelength regime, their electromagnetic response is typically dominated by dipolar (electric or magnetic) modes, with quadrupolar contributions emerging only for the larger sizes. For this reason, we set *conv* = 1, resulting in truncation order in the range  $M \in [7,10]$  for  $x \in [1, 2]$ . Thus, up to 10 terms are considered in our calculations which is consistent with the relevant multipolar contributions for the CDS geometries analyzed.

## 2.2 Electromagnetic Modeling of Iris-gated Core-Double Shell Nanoparticles

The asymmetric ICDS architectures were analyzed using FEM simulations in COMSOL Multiphysics, by solving the heat diffusion equation. The workflow followed two sequential steps: (i) light–matter interaction and (ii) thermal transport. In the electromagnetic stage, Maxwell’s equations were solved using COMSOL radiofrequency module. The ICDS geometries were defined as embedded in water, and the surrounding simulation domain was enclosed within perfectly matched layers to suppress spurious reflections. Illumination was provided by a linearly polarized plane wave of intensity  $I=0.1 \text{ mW } \mu\text{m}^{-2}$ , a standard reference value widely employed in thermoplasmonic studies<sup>[8,15,19,20]</sup>. A free tetrahedral mesh was used,

with maximum element size constrained to  $\lambda/8$  to ensure accurate representation of near-field features and geometric curvature. Although values up to  $\lambda/5$  are often considered adequate for generic plasmonic systems<sup>[21]</sup>, a stricter meshing criterion was selected to ensure accuracy robustness across all ICDS designs. To validate the FEM results, independent simulations were performed using Lumerical FDTD, which relies on a rectangular mesh strategy and thus provides a complementary numerical assessment.

### 2.3 Thermal Modelling

Thermal simulations were carried out using the *heat transfer in solids* interface in COMSOL. The volumetric power density computed in the electromagnetic stage was taken as the heat source term in the diffusion equation. Heat flux boundary conditions were imposed at the system's outer surfaces of the domain, with transfer coefficients derived from the built-in Nusselt correlations for flat interfaces. Given the nanoscale dimensions, small fluid volumes, and moderate temperature increases involved, heat conduction was treated as the dominant transport mechanism in accordance with established thermoplasmonic literature. A detailed discussion of both the electromagnetic and thermal modelling strategies is provided in Sections I and II in the supplementary document.

## 3. Results and Analysis

### 3.1. Optical study of the precursor Core-Double-Shell reference structure.

**Figure 1a** illustrates the CDS architecture examined in this study. The structure consists of a glass core, a gold shell and an outer polymer layer. For the purpose of this work, the polymer coating is taken to be polydimethylsiloxane (PDMS), selected due to its glass-like refractive index and a low thermal conductivity. The geometry is defined by the core radius ( $r_c$ ), the gold thickness ( $\delta_{Au}$ ) and the polymer thickness ( $\delta_p$ ). The symmetry of this structure promises a high stability under rotations with respect to the plane of polarization and a core-shell-like electromagnetic response, since the polymer's refractive index is real.

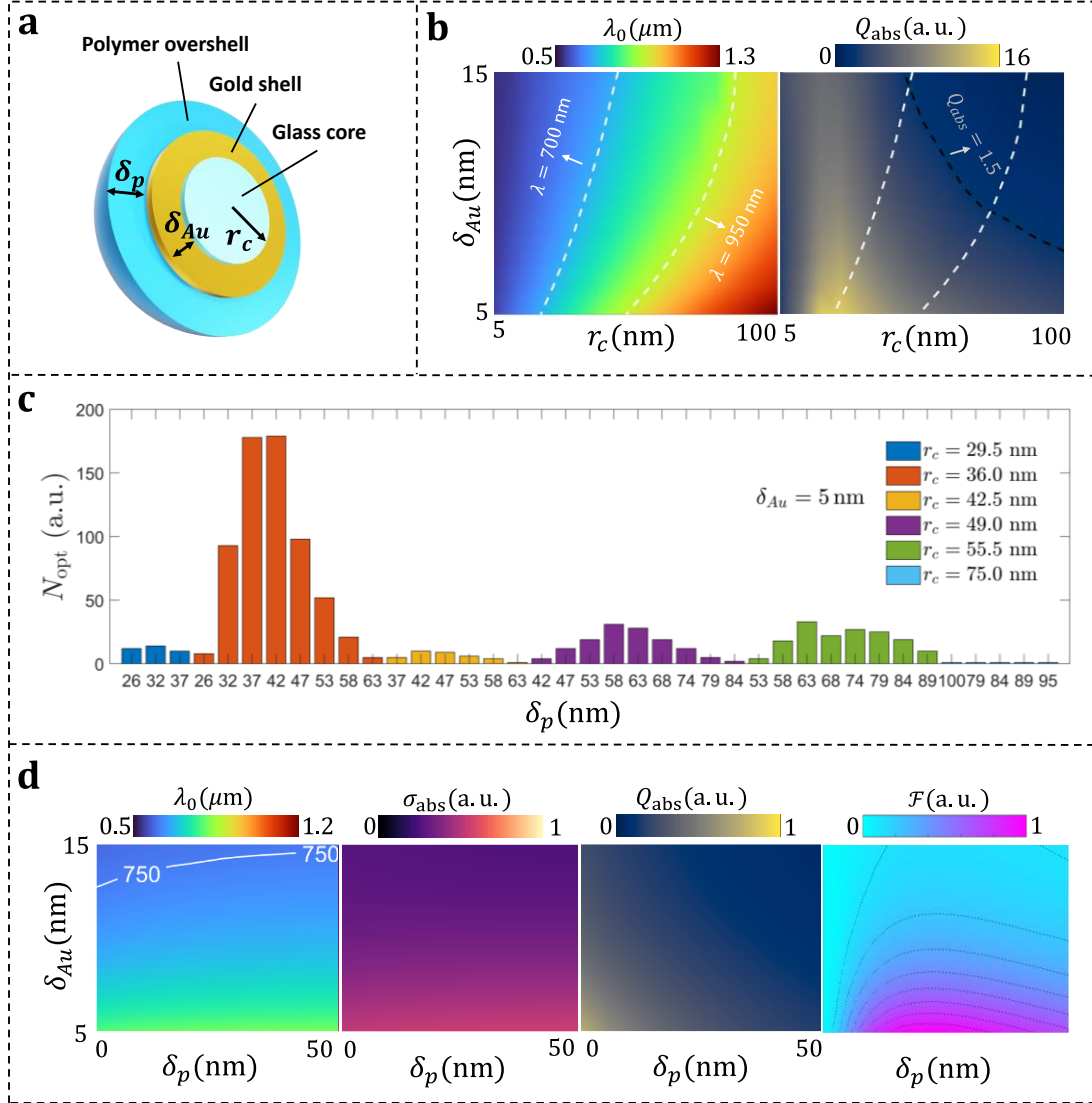


**Figure 1.** (a) Illustration of the structure under analysis defined by the core radius ( $r_c$ ), the gold thickness ( $\delta_{Au}$ ) and the polymer thickness ( $\delta_p$ ). The materials from the core to the overlayer are glass, gold and PDMS respectively. (b) Peak absorption wavelength (left) and absorption efficiency (right) for a traditional silica/gold core-shell as a function of  $\delta_{Au}$  and  $\delta_p$ . White and black dashed lines represent the first biowindow band and the limit for an absorption efficiency of 1.5, respectively. (c) Histogram with the absolute frequency ( $N_{opt}$ ) of optimal configurations for each gamma triplet ( $\gamma_1, \gamma_2, \gamma_3$ ) ranging from 1 to 1.5 as a function of  $r_c$  and  $\delta_p$ . (d) From left to right: peak absorption wavelength, peak absorption cross section, absorption efficiency and trade-off function in terms of  $\delta_{Au}$  and  $\delta_p$ .

Since the objective of this work is to identify geometries that simultaneously maximize heat generation within the first biological window (NIR-I) and enable spatially directional thermal transport, an initial selection of viable dimensional parameters is required. To this end, we first examined the electromagnetic response of conventional silica-gold core-shell (CS) nanoparticles by means of Mie theory<sup>[17]</sup>. Core radii in the range [5-100] nm with core shell thicknesses between 5 and 15 nm were performed to map the evolution of the plasmon

resonance wavelength and absorption efficiency. The results can be seen in Figure 1b. The analysis reveals that configurations with radii smaller than  $r_c \approx 23$  nm exhibit plasmonic resonances outside the NIR-I window, and are therefore unsuitable for photothermal applications in biological media. Similarly, structures with radii larger than  $r_c \approx 86$  nm show redshifted resonances and again fall outside the desired spectral region. Consequently, only structures with  $r_c \in (23, 86)$  nm satisfy the resonance-position requirement. Note that these numerical bounds arise from our discrete parameter sampling and should be interpreted with the understanding that small perturbations in the discretization would only induce marginal shifts in the resulting limits.

The absorption efficiency exhibits a non-monotonous dependence on particle size. A clear maximum occurs near  $r_c \approx 20$  nm for a gold shell thickness of  $\delta_{Au} \approx 5$  nm, whereas efficiencies drop for core radius  $r_c < 18$  nm. For larger radii, efficiency falls below 1.5 once core radius  $r_c > 75$  nm. This behaviour is consistent with the spectral absorption cross sections shown in Figure S1 for core radii of 5nm and 80nm. It can be observed that the maximum absorption reduces and the resonance blue-shifts approaching to the response of a solid metallic sphere, decreasing its absorption cross-section. Despite this trend, the smallest structure shows low absorption with the resonance out of the biowindow. On the other hand, thicker gold layer shell particles resonances fall within the first biowindow but display poor absorption performance due to their larger size. Balancing resonance position and absorption efficiency considerations therefore constrains the feasible parameter space to  $r_c \in [10, 75]$  nm and  $\delta_{Au} \in [5, 15]$  nm. These bounds, derived from CSs analysis, are also applied to the CDS study since the overshell is made of PDMS and therefore their responses are expected to follow the same plasmonic trends.

The electromagnetic response of the CDS structures was investigated using Mie theory, with the aim of identifying configurations that maximize the total temperature rise, the thermal directionality and heating efficiency. Achieving these goals, requires simultaneously maximizing absorption metrics, favoring small structures, and ensuring sufficiently thick polymer overshell to enable asymmetric temperature profiles<sup>[15]</sup>.

To systematically evaluate the balance between these competing properties, we define the following trade-off function:

$$\mathcal{F} = \bar{\sigma}_{abs}^{\gamma_1} \bar{Q}_{abs}^{\gamma_2} \bar{\delta}_p^{\gamma_3} \quad (1)$$

Where  $\bar{\sigma}_{abs}$ ,  $\bar{Q}_{abs}$  and  $\bar{\delta}_p$  are the normalized absorption cross section, absorption efficiency and quadratic polymer thickness. Normalization is performed with respect to the global maximum observed for each quantity. Since the relative weighting of these parameters cannot be assumed a priori, and given that their magnitudes vary slowly and non-uniformly across the design space for larger structures (see Figure S3), we introduce three exponents  $(\gamma_1, \gamma_2, \gamma_3)$  ranging from 1 to 1.5, chosen to prevent dominance by any single parameter and to preserve balanced multi-objective optimization. For every triplet  $(\gamma_1, \gamma_2, \gamma_3)$ , the global maximum of  $\mathcal{F}$  is computed, and the configuration yielding the global maximum is identified in each case. This enables a frequency-based analysis, revealing the most recurrent optima and defining a robust design space, an appropriate strategy given that no single polymer thickness is expected to be universally optimal due to the passive nature of thermal transport.

The results of this frequency-based analysis are presented in Figure 1c, where the histogram displays the number of times each CDS configuration (x-axis) emerges as a global optimum (y-axis). Remarkably, it can be observed that, in all cases, the global maximum is achieved for configurations with a gold shell thickness of 5 nm. This trend is consistent with the behaviour shown in Figure S2, where the absorption cross-section exhibits minimal sensitivity to polymer coating thickness variations but increases significantly as the gold shell becomes thinner. The consistent minimum of 5 nm is imposed by the fact that at this scale, the dielectric function of gold requires corrections for electron-surface scattering and cannot be reliably represented using bulk optical constants. A detailed discussion of the trade-off function and the associated convergence analysis is provided in Section I of the Supplementary Information.

The histogram in Figure 1c also shows that CDSs with either very small core radii ( $r_c = 29.5$  nm) or very large ones ( $r_c = 75$  nm) appear only with minimal frequency. As previously discussed, particles with small cores behave qualitatively more like homogeneous metallic spheres and therefore exhibit weak absorption, often outside the biowndows. On the other hand, the largest structures display relatively high absolute absorption but suffer from very low absorption efficiencies, which results in their marginal presence in the histogram. As a result, these geometries appear only for specific combinations of the exponents  $(\gamma^1, \gamma^2, \gamma^3)$  in the trade-off function. For example, efficiency optima may occur if,  $(\gamma_1, \gamma_2, \gamma_3) = (1, 1.5, 1)$ , whereas other choices such as  $(\gamma_1, \gamma_2, \gamma_3) = (1.5, 1, 1.5)$  may prioritize absorption and polymer-thickness contributions.

A closer examination reveals that, for each core radius, the global optima tend to concentrate around intermediate polymer thickness values. However, the highest frequency corresponds to core radius of  $r_c = 36$  nm, with preferred polymer thickness values in the range  $\delta_p \in [32, 53]$  nm. These observations indicate that the most favourable configurations generally combine moderate core sizes, thin gold shells ( $\delta_{Au} = 5$  nm), and polymer coatings of intermediate thickness.

To illustrate these trends, Figure 1d presents a detailed full Mie theory analysis for the most representative configuration identified in Figure 1c ( $r_c = 36$  nm). The results indicate that the plasmonic resonances of the evaluated geometries remain predominantly within the first biological window. The resonance wavelength is determined primarily by the gold shell thickness and exhibits only a slight redshift with increasing the polymer coating thicknesses evidenced by the almost horizontal pattern. An analogous trend is observed for the absorption cross section. This behaviour is expected, as the dominant absorption mechanism arises from the plasmonic mode from the interaction between light and the free electrons of the gold shell. Hence, variations in polymer layer induce secondary effects relative to changes in gold shell thickness, with the largest absorption generally achieved at  $\delta_{Au} = 5$  nm.

When absorption is examined in terms of efficiency, the interplay becomes more relevant. Thinner gold layers yield higher efficiencies, but larger overall structure sizes tend to penalize efficiency. As a result, the most efficient configurations occur near the lower ends of both the  $\delta_{Au}$  and  $\delta_p$  axes. Finally, in the trade-off function map (bottom panel of Fig 1d), these competing influences manifest clearly. The trade-off function increases steeply for thin gold layers, as expected from the absorption behaviour. However, a pronounced region of high values emerges at intermediate polymer thicknesses, reflecting the joint optimization of efficiency and normalized polymer volume. While efficiency alone generally favours the smaller structures, the polymer thickness criterion rewards thicker coatings, thereby shifting the optimum toward moderately larger structures.

Taken together, these results show that although very thin polymer layers might appear optimal based solely on optical performance, such geometries do not adequately support the thermal directionality and temperature enhancement requirements of this work. Instead, balanced designs with moderately thick polymer coatings provide the most favourable compromise

across absorption metric, efficiency considerations, and anticipated thermal behaviour, justifying their selection for subsequent electromagnetic and thermal analyses.

### 3.2. Opto-thermal study of the Iris-gated Core-Shell-Shell nanoparticle.

In the previous section, we examined a fully symmetric multilayered spherical nanoparticle, effectively a core–shell–shell nanoparticle from a plasmonic perspective. Owing to its complete spherical symmetry, such a structure cannot exhibit spatial thermal asymmetry, neither its near field electromagnetic distribution nor the results conductive heat flux, i.e, none of them can break rotational symmetry. As a consequence, the steady-state temperature field is strictly isotropic. Therefore, to break this symmetry and induce anisotropic heat conduction in the near-field, and given the passive character of thermal relaxation, structural asymmetry must be introduced.

According to the literature on thermoplasmonic anisotropy<sup>[14–16,22]</sup>, one of the most direct approaches to induce thermal asymmetry is to spatially modulate the heat source itself (i.e., the plasmonic absorption). However, this strategy typically requires complex nanoparticle synthesis and may reduce fabrication feasibility. In the present work, we instead introduce asymmetry exclusively in the polymer coating. This approach preserves the high symmetry of the underlying silica/gold core–shell configuration while enabling directional thermal transport with minimal structural perturbation.

Figure 2a schematically illustrates the proposed design, denoted here as as Iris-gated Core-Shell-Shell nanoparticle. The structure maintains the same parameters as the CDS reference (e.g., core radius, gold shell thickness, and polymer properties), but incorporates an “eyelid-like” aperture, i.e, an opening angle that defines the extent of the polymeric coverage. This opening is defined by a polar half-angle, corresponding to the spherical cap removed from the polymer coating. A 3D rendering and a 2D cross-section (left panels) clarify the geometry, while the right panel shows a sequence of ICDS structures with increasing opening angles, outlining the overall study workflow.

For the opto-thermal analysis, we consider polymer shell thicknesses from 0 to 60 nm surrounding a silica core of radius  $r_c = 36$  nm and a gold shell of 5 nm, consistent with the optimal dimensions identified from the multi-objective screening shown in the histogram of

Figure 1c. Figure 2b presents three colormaps summarizing key metrics as functions of polymer thickness and opening angle: resonance wavelength (left), peak absorption cross-section (center), and the temperature rise (right).

A clear and coherent trend is observed. As the opening angle increases, i.e., the polymeric coverage decreases, the resonance wavelength undergoes a progressive blueshift, approaching the response of a conventional core–shell structure. This behavior is consistent with the fact that PDMS has a refractive index higher than that of the surrounding medium (water); thus, its presence induces a redshift. As the polymer layer diminishes, so does its optical influence. The absorption cross-section exhibits a similar dependence: within the quasi-static regime, absorption scales with the effective permittivity of the surrounding medium. Accordingly, polymer rich configurations (smaller opening angles and thicker coatings) enhance electromagnetic coupling and yield larger absorption cross sections.

The thermal response (Figure 2b, right), mirrors these optical trends. A thicker polymer layer combined with a smaller opening angle produces a larger temperature increase. This effect can be explained by the low thermal conductivity of PDMS, approximately six times lower than that of water. A thicker polymer coating therefore enhances local thermal insulation and leads to stronger local heating. Likewise, a narrower opening angle increases the degree of confinement, further elevating the steady-state temperature.

Across the explored configurations, temperature increments exceeding 10 K are observed under the reference illumination conditions. This magnitude of heating is compatible with the typical hyperthermia threshold in biological environments<sup>[23]</sup>, indicating that the proposed ICDS nanostructures are viable candidates for localized photothermal applications. Nevertheless, it should be emphasized that practical implementations would require collective heating effects in dense colloidal suspensions to exceed hyperthermia thresholds robustly, a general limitation inherent to nanoparticle level thermoplasmonics rather than a shortcoming of the ICDS nanostructure itself.

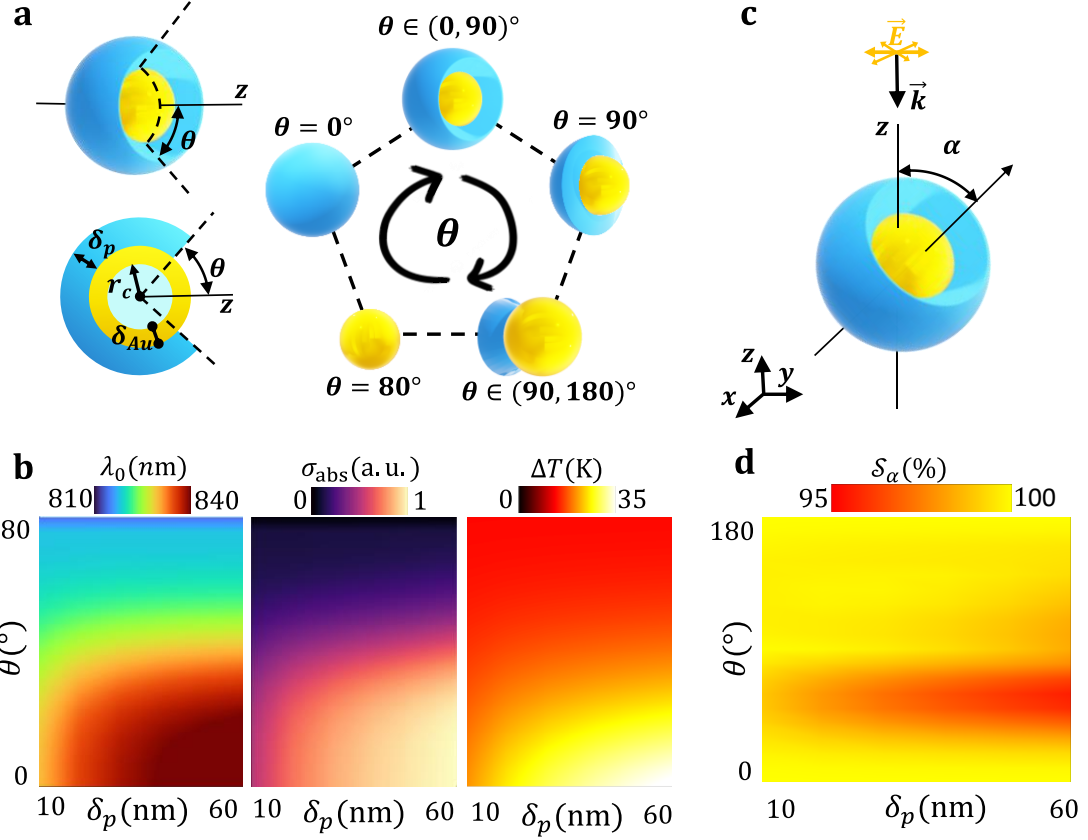


Figure 2. a) Illustration of the ICDS and the procedure followed in the analysis.  $\theta$  is the semi-angle, measured from the centre of the particle, that defines the iris with respect to the z-axis. b) Resonance wavelength, absorption cross section and temperature increase maps as a function of the aperture angle  $\theta$  and the polymer thickness  $\delta_p$ . c) Schematic representation of the unpolarized plane wave illuminating the ICDS at an angle  $\alpha$ , defined as the angle between the incident wavevector  $\vec{k}$  and the z-axis. d) Stability map (equation 2) as a function of the aperture angle  $\theta$  and the polymer thickness  $\delta_p$ .

As discussed previously, the structural design proposed in this work was intentionally conceived to incorporate only the minimal degree of spatial asymmetry required to induce anisotropic thermal flux, while keeping the overall geometry as simple as possible to facilitate experimental fabrication. However, the working hypothesis of this study assumes that these nanostructures are intended for biomedical applications, specifically in the context of thermoplasmonic hyperthermia for cancer treatment. In such environments, nanoparticles are freely suspended in a fluid medium and undergo random rotations. Moreover, the incident illumination may experience partial or even complete depolarization as it propagates through biological tissue. These factors may reduce the effectiveness of any design whose optical performance is strongly orientation dependent.

For this reason, we evaluated the impact of particle rotational orientation on the absorption performance of each ICDS configuration, considering both polymer shell thickness and opening angle. The strategy followed, depicted in Figure 2c, mirrors the approach of the previous section: the opening angle  $\theta$  is systematically varied, and for each geometry, all possible rotational angles  $\alpha$  are examined. Owing to the high symmetry of the ICDS design, the full set of all possible rotations can be reduced to a rotation around the x-axis with  $\alpha \in [0, 180]^\circ$ , without loss of generality.

For every configuration, the absorption cross-section was computed at the optimal excitation wavelength, i.e., the one that maximized absorption when the structure is perfectly aligned, with the iris oriented perpendicular to the direction of beam propagation (incident light traveling along the negative z-axis). This choice corresponds to the best-case optical response, as identified in the resonance wavelength map shown in Figure 1b.

To quantify the absorption sensitivity of each structure to rotational misalignement, i.e., misalignment between the particle iris and the incident electric field, we introduced a stability metric defined as the maximum relative deviation in absorption across all sampled orientations for a given structural configuration ( $\theta, \delta_p$ ):

$$\mathcal{S}_\alpha = \left( 1 - \frac{\min\{\sigma_{abs}(\alpha_i)\}_{i \in I}}{\max\{\sigma_{abs}(\alpha_i)\}_{i \in I}} \right) \cdot 100 \quad (2)$$

where  $\sigma_{abs}(\alpha_i)$  is the absorption cross-section for orientation  $\alpha_i$ . This metric thus provides a quantitative estimation of the maximum change in absorption induced by particle reorientation for each structural configuration. The resulting absorption stability is presented in the color map of Figure 2d, as defined in Equation 2, plotted as a function of the polymer shell thickness and the opening angle.

The results show that, in general, the stability remains remarkably high, between 95% and 100% across all studied configurations. This demonstrates that the proposed ICDS design exhibits a remarkably robust optical response against rotational misalignment, which constitutes a significant advantage over other geometries reported in the literature<sup>[8,24]</sup>. While, several anisotropic geometries have been explored, including rods, disks, and toroidal particles, with the latter often exhibiting the best photothermal conversion efficiencies<sup>[4,8]</sup>, their optical performance is highly sensitive to particle orientation. In contrast, the ICDS typically offers a lower absorption but strong rotational stability.

The colormap in Figure 2d reveals that the highest stability is achieved for configurations in which the metallic surface is either extensively covered or barely covered by the polymeric layer, i.e., for a large or short iris, respectively. This trend is expected, as these extreme cases closely resembles a fully symmetric particle, either approaching the conventional core–shell or the reference core–shell–shell geometry. In both cases, minimal asymmetry leads to strongly orientation-invariant optical behaviour.

On the other hand, a distinct region of reduced rotational stability is observed for iris with opening angles between approximately  $30^\circ$  and  $90^\circ$ . Within this range, structures with thicker polymer coatings exhibit a slightly larger decrease in stability. As previously discussed, the plasmonic response is highly sensitive to the refractive index of the surrounding medium. When the metallic surface is only partially covered (i.e., large iris), the structure behaves similarly to a conventional core–shell particle, and the influence of the polymer is minimal. In contrast, for opening angles below  $90^\circ$ , a significant portion of the metallic surface is embedded within the polymer layer. This increases both the optical impact of its refractive index and the increase of the intrinsic geometric asymmetry of the system. This explains why the region of minimum stability is shifted toward smaller opening angles.

From the optical analysis of the ICDS structures, it follows that the reference configuration composed of a 36 nm silica core, a 5 nm gold shell, and a polymer thickness in the range 30 - 50 nm constitutes a promising design choice. This configuration demonstrates the highest combined optical figure of merit and, as illustrated in Figure 2, maintains a broad range of opening angles for which both the absorption magnitude and rotational stability remain high. Furthermore, the resonance wavelength for this set of parameters range remains within the first therapeutic window, exhibiting only modest redshifts, typically no larger than  $\sim 30$  nm, relative to the fully symmetric CDS structure.

Therefore, based only on optical considerations, the most promising ICDS designs are those defined by the parameter set:  $(r_c, \delta_{Au}, \delta_p) = (36, 5, 30 - 50) nm$  and partially covered within the range  $\theta \in [0^\circ, 90^\circ]$ . These designs are, *a priori*, compatible with the ultimate objective of this work: achieving controlled thermal directionality and thermal focusing while preserving structural simplicity and rotational robustness.

### 3.3. Analysis of the thermal flux in the stationary regime.

To determine more precisely the acceptable range of opening angles of thermal asymmetry, we perform an analysis of the conductive thermal flux analysis in the stationary regime. For this purpose, we introduce the concept of thermal focusing. Although this notion shares terminology with geometrical optics, its interpretation here is different. In the present context, thermal focusing refers to the redistribution of conductive heat power across a predefined control surface, compared to the fully symmetric reference case.

This concept is illustrated in Figure 3a. The ICDS nanostructure under study is enclosed within a concentric spherical control surface  $\mathbb{S}^2$ , positioned at a fixed distance from the outer surface of the particle. This distance  $\Delta$  is defined as the difference between the radius of the control sphere and the outer radius of the nanostructure. Given the biomedical orientation of this work, particularly in thermoplasmonic hyperthermia, we assume that nanoparticles are biofunctionalized and adhered to cell membranes. Accordingly, we set  $\Delta = 15$  nm, consistent with the typical size of antibody-functionalized gold nanoparticles<sup>[25]</sup>. This value may vary depending on the functionalization agent; while different values could be explored, and may slightly modify the heat flux magnitudes, similar qualitative trends and overall conclusions are expected.

Formally, we compute the relative thermal power crossing a spherical surface defined by a solid angle  $\Omega(\beta)$ , where  $\beta$  is the polar half-angle that substends the cap of the control sphere. By sweeping over  $\beta$  from  $0^\circ$  to  $180^\circ$ , we obtain the power fraction function  $\eta(\beta)$ , defined as:

$$\eta(\beta) = \frac{\iint_{\Omega(\beta)} \vec{\Phi} \cdot \vec{n} dS}{\iint_{\mathbb{S}^2} \vec{\Phi} \cdot \vec{n} dS} \quad (3)$$

Where  $\vec{\Phi}$  is the conductive heat flux and  $\vec{n}$  the outward normal to the surface. When  $\beta < 90^\circ$ , the integration domain corresponds to a spherical cap smaller than the upper hemisphere of the control surface. For  $\beta > 90^\circ$ , the integral includes the entire upper hemisphere and a portion of the lower hemisphere. This formulation enables a direct quantification of directional thermal emission and constitutes the basis of our thermal focusing analysis.

Based on the results obtained in the previous optical studies, we select a polymer thickness of  $\delta_p = 40$  nm, which provides favourable results in terms of absorption, resonance wavelength, temperature, and rotational stability, while also maximizing the overall figure of merit. With

this parameter fixed, we evaluate whether a specific value or an interval of opening angles can induce thermal asymmetry and thereby enhance the anisotropy of the conductive heat flux in the near field of the ICSD nanoparticle.

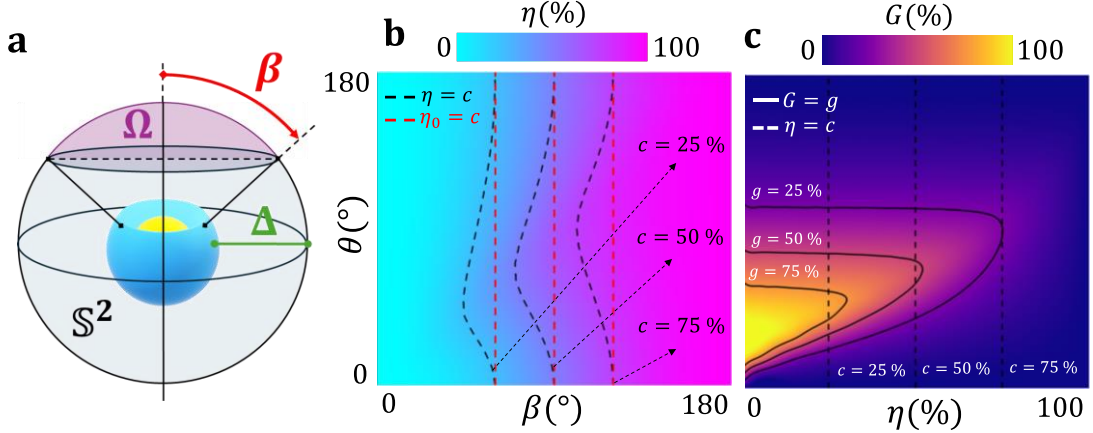


Figure 3. a) Geometrical construction employed to quantify the directional response of the ICDS nanoparticle. The total outward power is collected over the closed integration control surface  $\mathbb{S}^2$ . A spherical cap of semi-aperture  $\beta$  (purple domain with solid angle  $\Omega$ ) is used to evaluate the power fraction  $\eta$ . The control surface  $\mathbb{S}^2$  is located at a distance  $\Delta = 15$  nm to the ICDS surface. b) Map of  $\eta(\beta, \theta)$  expressed in percentage. Black dashed curves trace the regions where the power fraction is constant with  $\eta = 25, 50, 75\%$ , while red dashed curves indicate the corresponding values for the symmetric case. c) Gain map  $G(\eta, \theta)$ . Solid black isolines mark the regions with constant gain for 25%, 50%, and 75%; vertical dashed lines highlight the regions along which the power fraction  $\eta$  is constant with the same percentages.

The results of this analysis, carried out following the methodology illustrated in Figure 3a, are presented in Figure 3b, c. Since the objective is to analyse thermal directionality, Figure 3b also displays equienergetic contours for which the power fraction reaches 25%, 50%, and 75% of the total generated power (indicated by black dashed lines). For comparison, red dashed lines highlight the integration angles  $\beta$  at which these same power levels are reached in the fully symmetric case (i.e.,  $\theta = 0^\circ$  and  $\theta = 180^\circ$ ). For further details on the symmetric case analysis and the corresponding flux distribution, refer to the section 2 in Supplementary Information.

In general, the equienergetic contours for asymmetric ICDS structures are consistently shifted to the left of those corresponding to the symmetric reference lines. This means that, for any given power fraction, the integration angle  $\beta$  required to enclose that power is smaller in the asymmetric case. In other words, the asymmetric particle concentrates a given amount of thermal power within a smaller spherical region than the symmetric CDS configuration. Thus, the same power is redistributed over a reduced surface area. This clearly demonstrates that any

degree of asymmetry in the ICDS design, regardless of how subtle is, induces thermal directionality.

As expected, the function  $\eta(\beta)$  increases monotonically from 0% to 100% as  $\beta$  approaches  $180^\circ$ , in accordance with energy conservation over the full spherical surface. To identify a suitable opening angles range, we focus on configurations that maximize thermal directionality at a 50% energy fraction, which corresponds to thermal energy propagation across the entire upper hemisphere in a fully symmetric system. As shown in Figure 3b, the largest deviations from the symmetric case occur for ICDS structures with an iris in the range  $\theta = [60, 80]^\circ$ . For these geometries, the fraction of power directed toward the upper hemisphere ( $\beta = 90^\circ$ ) increases significantly, revealing a pronounced thermal redirection effect. Because this redistribution forces the same amount of energy through a smaller area, it naturally leads to a local enhancement of the surface power density.

To quantify this thermal focusing effect, we introduce a thermal focusing gain function in terms of the power fraction, defined as the relative increase in energy surface density produced for a given power fraction. For each value of  $\eta$ , the surface area required to transmit that fraction is compared between the ICDS structure and the symmetric case. The complete mathematical formulation is provided in Section 3 of the Supplementary Information and can be expressed as:

$$G(\eta, \theta) = \left( \frac{1 - \cos(\beta_\theta(\eta))}{1 - \cos(\beta_0(\eta))} - 1 \right) \cdot 100 \quad (4)$$

where the function  $\beta_\theta(\eta)$  is the integration angle corresponding to the power fraction  $\eta$  for an ICDS nanoparticle with specific iris of  $\theta$ , and  $\beta_0(\eta)$  is the equivalent angle for the symmetric case. This metric therefore quantifies the degree of power concentration achieved by the asymmetric design relative to the fully symmetric configuration,  $\theta = 0^\circ$ .

Figure 3c is built by applying Equation 4 to the data obtained in Figure 3b. In all cases, the gain is strictly positive, indicating that even weak asymmetries result in some degree of thermal densification. In general, the gain increases as the iris becomes smaller (i.e., larger polymer coverage), consistent with the stronger asymmetry introduced by a more extended insulating region. However, a pronounced maximum is observed for moderate opening angles, which is explained by the non-trivial dependence of  $\beta_0$  on both the polymer thickness and the geometric aperture. As shown in Figure 3b, for each power fraction, there exists an optimal opening angle

that maximises the difference between  $\beta$  and  $\beta_0$ . This gives rise to the bell-shaped envelope observed in Figure 3c. This behaviour can be understood because of the polymer covering influence. Larger polymer coverages (smaller  $\theta$ ) produce stronger directionality but mainly for small  $\beta$ . Conversely, reduced polymer coverages (larger  $\theta$ ) translate into weaker directionality that manifest predominantly at larger  $\beta$ . This interplay between these regimes naturally leads to an optimal region for intermediate opening angles.

Since our goal is to enhance heat dissipation toward the upper hemispace, we again consider a power fraction  $\eta = 50\%$  as a reference. In this case, the data reveal a well-defined region with opening angles in the range  $\theta = [60, 80]^\circ$  where the focusing gain exceeds 1.5, indicating that 50% of the total power is concentrated over a surface 35% smaller than in the symmetric case. This translates into an increase of over 50% in surface power density, compared to the symmetric case.

Taking all metrics into account, temperature rise, flux anisotropy, focusing efficiency, rotational stability, and multi-objective optical performance, we report that ICDS structures with irises of  $\theta = [60, 80]^\circ$  provide the most balanced overall response. Specifically, these configurations yield: (i) a maximum temperature rise of approximately 20-23°C, (ii) a power fraction directed toward the upper hemisphere ( $\beta = 90^\circ$ ) of up to  $\eta = 67\%$ , (iii) a focusing gain for the upper hemisphere of  $G = 35\%$ , meaning the surface power density across the upper hemisphere is 1.35 times greater than in the fully symmetric configuration and (iv) they concentrate the half of the total thermal energy a 50% more than the fully symmetric structure. In other words, at  $\eta = 50\%$ , this structure achieves a focusing gain  $G \approx 50\%$ , effectively delivering 1.5 times the surface power density compared to the symmetric case.

Altogether, these findings indicate that the ICDS particle defined by  $(r_c, \delta_{Au}, \delta_p, \theta) = (36 \text{ nm}, 5 \text{ nm}, 40 \text{ nm}, 70^\circ)$  offers an optimal compromise between thermal directionality power densification, optical performance, and structural simplicity. It is worth highlighting that, based on our analysis, particles defined by  $(r_c, \delta_{Au}, \delta_p, \theta) = (36 \text{ nm}, 5 \text{ nm}, 30 - 40 \text{ nm}, 60 - 80^\circ)$  are expected to provide similarly balanced and experimentally feasible responses as well.

### 3.4. Thermal directionality under pulsed illumination.

In the previous sections, we quantified the ability of ICDS structures to generate thermal asymmetry under continuous-wave (CW) illumination. However, many biomedical applications it is both common and advantageous to employ pulsed illumination because the structures are usually embedded in heterogeneous environments. Such heterogeneity implies a distribution of thermal relaxation times. Through proper pulse engineering, specific tissue components can be selectively heated while minimizing collateral damage, a well-established advantage of pulsed thermoplasmonics<sup>[26]</sup>.

Given the size and morphology of the ICDS structure, its characteristic heating and cooling times are estimated to fall within the nanosecond regime. Consequently, pulses much shorter than its characteristic time will interact with the particle as if it had significant thermal inertia, whereas considerably longer pulses will approach the CW limit. To determine the relevant structure's thermal time scale, we computed the characteristic heating time by fitting the transient temperature rise under CW illumination to an error-function time profile, following established models<sup>[1]</sup>. As shown in Figure S5, this procedure yields a characteristic heating time of approximately 30 ns.

To ensure a meaningful comparison with the CW results reported above, the pulse fluence was chosen such that the time averaged power density equals the reference value of  $0.1 \text{ mW } \mu\text{m}^{-2}$ . This requirement corresponds to a fluence of  $0.3 \text{ mJ cm}^{-2}$ .

Figure 4a presents the absorbed power (left) and the corresponding temperature at three points of interest (right) as functions of time. A delay of approximately 1 ns between energy absorption and the resulting temperature rise is observed. This temporal delay can be attributed to the thermal inertia of the particle, since the absorption of the electromagnetic energy is typically faster than heat dissipation<sup>[7]</sup>.

As depicted in the inset of Figure 4a, temperatures were monitored at three representative locations to assess the degree of thermal asymmetry under pulsed excitation. The first point corresponds to the maximum temperature within the gold shell (solid line). The other two points were placed along the symmetry axis, 15 nm away from the rear and front sides of the structure. This distance was selected as a reference because it corresponds to the expected separation between the bio-functionalized particles and a cell membrane. Under pulsed excitation, the temperature at the reference point (front) decreases from more than  $15 \text{ } ^\circ\text{C}$  to approximately

8 °C as the pulse decays. Notably, the temperature drop across the dielectric polymer layer between the gold shell and the rear reference point, exceeds 13 °C, confirming the thermal insulation effect produced by the low conductivity dielectric coating. This insulating barrier suppresses heat transfer toward the rear hemisphere. By contrast, the temperature difference between the front and rear reference points is more modest, around 8 °C, indicating that significant thermal energy is preferentially directed towards the front side, consistent with the behaviour observed under CW illumination.

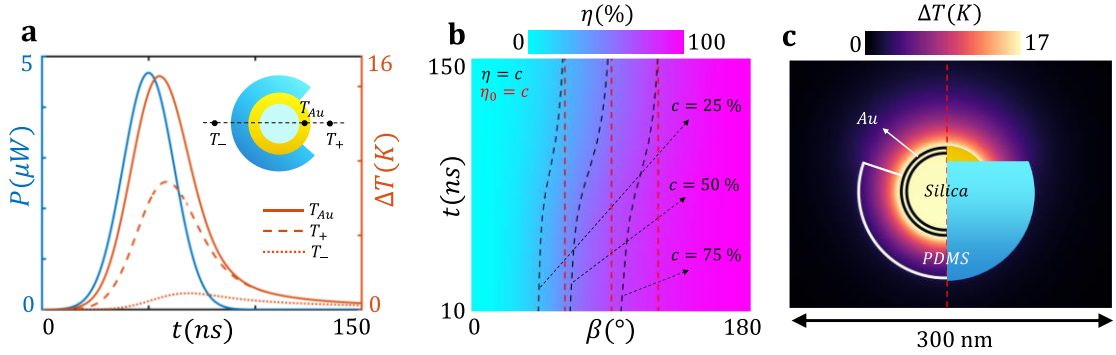


Figure 4. Time evolution of the total power dissipated in the gold shell (blue curve, left axis) and the corresponding temperature increases at three key locations: in the gold shell itself ( $T_{Au}$ ), in the exposed direction at 15 nm from the Au surface ( $T_+$ ), and in the shielded region over the control surface ( $T_-$ ). The inset illustrates the geometric location of these points over the ICDS nanoparticle. b) Power fraction  $\eta(\beta, t)$ . Black dashed curves indicate the condition  $\eta = c$ , while red dashed curves correspond to  $\eta_0 = c$ , for coverage fractions  $c = 25\%$ ,  $50\%$ , and  $75\%$ . c) Temperature map at the instant when the gold shell reaches its maximum temperature. The left half displays the computed temperature field, while the right half is overlaid with a schematic of the nanoparticle cross-section, showing the internal layers (Au and PDMS) and delimiting the physically inaccessible domains.

A progressively increasing temporal delay between the three temperature traces is also observed. The delay between the temperature peak in the gold shell and that at the front reference point is smaller because the latter is in water, which exhibits higher thermal conductivity. In contrast, the rear reference point is separated from the gold by a PDMS shell, whose low thermal conductivity slows down the heat transfer process. As a result, the structure consistently produces a pronounced front–rear temperature contrast and effectively insulates the rear region, preventing it from reaching elevated temperatures throughout the entire illumination period.

Based on the analysis of Figure 3, one would expect the anisotropy of the heat flux to evolve over time. To examine this behaviour, we performed an analysis analogous to that shown in Figure 3b, now resolved in time. Specifically, we computed the time dependent power fraction

by integrating the instantaneous heat flux over spherical regions defined by the solid angle  $\Omega(\beta)$ , sweeping  $\beta$  from  $0^\circ$  to  $180^\circ$ . These results are shown in Figure 4b.

The resulting equienergy curves reveal that, at all times, the ICDS nanoparticle exhibits greater directional heat redistribution than the symmetric reference. The curves associated with the asymmetric structure remain consistently shifted to the left, confirming that the ICDS geometry induces asymmetric heat flux under pulsed excitation just as it does under continuous illumination.

However, the degree of thermal directionality diminishes as time increases. Under pulsed excitation, the equienergy curves of the ICDS nanoparticle gradually converge toward those of the symmetric particle. This reduction in asymmetry is most pronounced during the thermal relaxation phase, after the optical excitation has ceased. Such behaviour is expected because the pulse duration is on the order of the characteristic heating time of the particle. Once the external excitation ends, heat diffusion drives the system toward equilibrium, and thermal relaxation leads to a spatial homogenisation of the temperature field. Consequently, the thermal asymmetry persists only during the pulse and is progressively lost as the system relaxes.

Finally, Figure 4c shows the temperature map produced by the ICDS nanoparticle at the moment when the gold shell reaches its peak temperature. A pronounced hot spot emerges adjacent to the exposed aperture (iris region), creating an extended and easily accessible heated volume within the external medium. This region is particularly relevant in biomedical contexts, as therapeutic agents or biological targets located near the aperture can experience efficient and localized heating. In contrast, the PDMS over-layer efficiently insulates the regions shielded by the polymer coating, preventing undesired temperature increases in areas that are intended to remain unaffected.

To facilitate interpretation, the right half of the temperature map is complemented with a cut-away schematic of the nanostructure, explicitly marking the Au and PDMS domains and delineating the boundaries that are inaccessible to the surrounding fluid. This composite visualization highlights how the anisotropic polymer coating selectively directs heat toward the aperture while maintaining thermal protection over the remaining particle surface. Despite its minimalistic architecture, the ICDS design exhibits strong thermal asymmetry and pronounced directional intensification, all while retaining mechanical robustness and geometric simplicity, that greatly facilitate experimental fabrication. These combined properties position the ICDS

design as a particularly promising candidate for plasmonic hyperthermia-based cancer therapies, where controlled, directional, and localized heat delivery is essential.

#### 4. Conclusions

In this work, we have presented a computational methodology and a multi objective figure of merit tailored to simultaneously evaluate the optical and thermal performance of multilayered nanoparticles. Our proposed framework combines generalized Mie theory with full-wave numerical simulations, enabling a systematic and efficient exploration of the multidimensional design space. Importantly, both the figure of merit and the computational workflow are formulated in a generalizable manner, making them readily extensible beyond the specific case of CDS nanoparticles to a broad range of plasmonic and hybrid architectures.

We also defined a thermal gain parameter, a metric that quantifies the degree of thermal intensification and complements the conventional interpretation of thermal directionality. By establishing a direct connection between directional heat flux and surface power density, this parameter provides a more rigorous description of anisotropic thermal transport in nanoscale systems. This link between directionality and densification of thermal energy, offers a robust physical criterion for evaluating and comparing candidate structures that optimize directional heating.

Among the wide set of candidate configurations evaluated, we identified an optimal ICDS design defined by  $(r_c, \delta_{Au}, \delta_p, \theta) = (36\text{ nm}, 5\text{ nm}, 40\text{ nm}, 70^\circ)$ . This structure delivers a maximum temperature increase of 20–23 °C, a thermal directionality of up to 67% of the total power flux toward the upper hemisphere, and a focusing gain of approximately 50%, corresponding to a 1.5-fold increase in surface power density compared to the symmetric case. Notably, this performance is achieved while maintaining a high degree of geometric simplicity and symmetry, ensuring excellent rotational stability, and facilitating practical fabrication. The combination of strong thermal asymmetry, directional focusing, optical robustness, and structural feasibility makes the ICDS design a promising candidate for experimental realization and photothermal therapy applications.

Finally, the rapid screening and analysis methodology developed in this work are expected to be of interest to both theorists and experimentalists working on the development of advanced specialized nanostructures. Beyond the specific case of plasmonic photothermal therapy, the

general framework can be readily adapted to other applications involving different operating wavelengths, materials, and performance constraints, including sensing, photocatalysis, energy harvesting, and nanoscale thermal management. As such, the approach presented here provides a versatile strategy for guiding design and optimization of next-generation thermoplasmonic technologies.

## Acknowledgements

P.A. acknowledges support by the Spanish Ministerio de Ciencia e Innovación under project MOPHOSYS (grant no. PID2022-139560NB-I00). J. G.-C. acknowledges J. Cachón and M. P. Ogáyar for the scientific discussions on heat transport in biological tissues.

## References

- [1] G. Baffou, *Thermoplasmonics*, Cambridge University, **2018**.
- [2] G. Baffou, R. Quidant, F. J. García De Abajo, *ACS Nano* **2010**, *4*, 709.
- [3] A. O. Govorov, H. H. Richardson, *Nano Today* **2007**, *2*, 30.
- [4] L. Jauffred, A. Samadi, H. Klingberg, P. M. Bendix, L. B. Oddershede, *Chem Rev* **2019**, *119*, 8087.
- [5] G. Baffou, F. Cichos, R. Quidant, *Nat Mater* **2020**, *19*, 946.
- [6] L. Labrador-Páez, E. C. Ximenes, P. Rodríguez-Sevilla, D. H. Ortgies, U. Rocha, C. Jacinto, E. Martín Rodríguez, P. Haro-González, D. Jaque, *Nanoscale* **2018**, *10*, 12935.
- [7] K. Metwally, S. Mensah, G. Baffou, *Journal of Physical Chemistry C* **2015**, *119*, 28586.
- [8] J. González-Colsa, G. Serrera, J. M. Saiz, D. Ortiz, F. González, F. Bresme, F. Moreno, P. Albella, *Opt Express* **2022**, *30*, 125.
- [9] J. T. Jørgensen, K. Norregaard, P. Tian, P. M. Bendix, A. Kjaer, L. B. Oddershede, *Sci Rep* **2016**, *6*, 1.
- [10] C. M. Maier, M. A. Huergo, S. Milosevic, C. Pernpeintner, M. Li, D. P. Singh, D. Walker, P. Fischer, J. Feldmann, T. Lohmüller, *Nano Lett* **2018**, *18*, 7935.
- [11] L. Zhao, X. Zhang, X. Wang, X. Guan, W. Zhang, J. Ma, *J Nanobiotechnology* **2021**, *19*, 335.
- [12] G. Agrawal, R. Agrawal, *ACS Appl Nano Mater* **2019**, *2*, 1738.
- [13] H. Su, C. A. Hurd Price, L. Jing, Q. Tian, J. Liu, K. Qian, *Mater Today Bio* **2019**, *4*, DOI 10.1016/j.mtbi.2019.100033.
- [14] J. D. Olarte-Plata, J. Gabriel, P. Albella, F. Bresme, *ACS Nano* **2022**, *16*, 694.
- [15] J. González-Colsa, A. Franco, F. Bresme, F. Moreno, P. Albella, *Sci Rep* **2022**, *12*, 14222.
- [16] J. González-Colsa, F. Bresme, P. Albella, *The Journal of Physical Chemistry C* **2023**, *127*, 19152.
- [17] J. Schäfer, MatScat (<https://www.mathworks.com/matlabcentral/fileexchange/36831-matcat>), *MATLAB Central File Exchange* **2025**.
- [18] P. B. Johnson, R. W. Christy, *Phys Rev B* **1972**, *6*, 4370.
- [19] G. Baffou, P. Berto, E. Bermúdez Ureña, R. Quidant, S. Monneret, J. Polleux, H. Rigneault, *ACS Nano* **2013**, *7*, 6478.

- [20] L. Khosravi Khorashad, L. V. Besteiro, Z. Wang, J. Valentine, A. O. Govorov, *Journal of Physical Chemistry C* **2016**, *120*, 13215.
- [21] COMSOL Multiphysics V6.1, Stockholm, COMSOL AB, **2022**, 90.
- [22] P. P. Yang, Y. G. Zhai, G. Bin Qi, Y. X. Lin, Q. Luo, Y. Yang, A. P. Xu, C. Yang, Y. S. Li, L. Wang, H. Wang, *Small* **2016**, *12*, 5423.
- [23] K. F. Chu, D. E. Dupuy, *Nat Rev Cancer* **2014**, *14*, 199.
- [24] F. Alali, I. H. Karampelas, Y. H. Kim, E. P. Furlani, *Journal of Physical Chemistry C* **2013**, *117*, 20178.
- [25] M. J. Pollitt, G. Buckton, R. Piper, S. Brocchini, *RSC Adv* **2015**, *5*, 24521.
- [26] L. Carroll, T. R. Humphreys, *Clin Dermatol* **2006**, *24*, 2.

## Supporting Information

### **Design Principles for Tailoring Heat Transport via Iris-Gated Core–Double–Shell Nanoparticles in the Context of Photothermal Therapies**

*Javier González-Colsa\*, Fernando Bresme, Pablo Albella\**

J. González-Colsa, P. Albella

Group of Optics, Department of Applied Physics, University of Cantabria, 39005 Santander, Spain.

E-mail: [javier.gonzalezcols@unican.es](mailto:javier.gonzalezcols@unican.es), [pablo.albella@unican.es](mailto:pablo.albella@unican.es).

F. Bresme

Department of Chemistry, Molecular Sciences Research Hub, Imperial College London, London W12 0BZ, UK.

#### **I.-Electromagnetic analysis of Core–Shell–Shell structures.**

To guide the selection of the structural parameters for the more complex core–shell–shell geometry, we begin by analysing a simpler system: the traditional core–shell nanoparticle. This simplification is justified by the fact that the overshell in the definitive design is composed of a polymeric material, which is expected to introduce only minor deviations in the absorption cross-section compared to the standard core–shell configuration. This is because the main absorption mechanism is predominantly governed by a plasmonic mode localized in the gold shell.

The design criterion employed is to target structures that resonate within the first biological transparency window (approximately 750–950 nm), which is optimal for biomedical applications such as photothermal therapy. This is one of the motivations for focusing on core–

shell structures, in addition to the fact that they admit fully analytical electromagnetic solutions, which facilitates both physical insight and computational efficiency.

Accordingly, the traditional core–shell geometry serves as a foundational model to elucidate the feasible parameter space and guide the preliminary selection of suitable configurations. Figure S1 illustrates the absorption cross-sections for a set of limiting cases. In panel (a), we show results for a core–shell nanoparticle with a fixed core diameter of 10 nm and varying gold shell thicknesses. As can be observed, the spectral response resembles that of a solid gold sphere, with thicker shells yielding higher absorption values. However, the overall absorption remains weak, and the resonance peaks lie outside the first therapeutic window. Based on these results, we conclude that configurations with small core sizes are suboptimal for our application, and we therefore focus on core–shell structures with larger core radii in subsequent analyses.

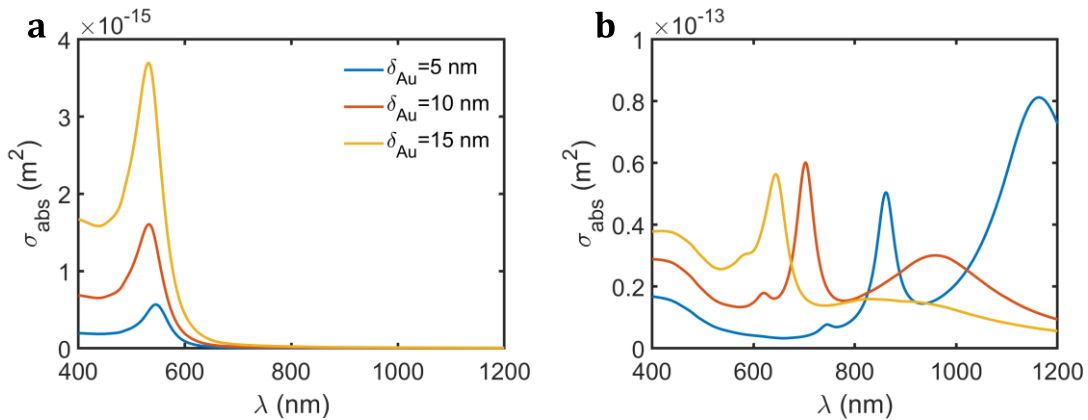


Figure S1. Spectral absorption cross sections for  $\delta_{Au} = 5, 10, 15$  nm in the case of  $r_c = 5$  nm (a) and  $r_c = 80$  nm (b).

In contrast, panel (b) of Figure S1 presents the absorption cross-section for a core–shell nanoparticle with a large core diameter of 160 nm. As shown, when the gold shell is only 5 nm thick, the plasmonic resonance lies far beyond the second biological transparency window (typically defined between 1000–1400 nm). Although the resonance shifts back toward the therapeutic window for thicker gold coatings, its magnitude is significantly lower.

Despite the fact that such large structures can exhibit strong absolute absorption, their absorption efficiency, defined as the absorption cross-section normalized by the geometrical cross-section, is expected to be low. In some cases, it may even fall below the efficiency of smaller structures due to the relatively larger volume that does not contribute effectively to

plasmonic heating. For this reason, core radii larger than 160 nm are determined suboptimal and will not be considered further in the design set.

About the gold shell thickness, we define 5 nm and 15 nm as practical lower and upper bounds, respectively. Shells thinner than 5 nm require semi classic corrections to the dielectric function due to surface electron scattering effects<sup>[1]</sup>, which complicate both modelling and interpretation. On the other hand, gold shells thicker than 15 nm tend to induce a spectral blueshift in the plasmonic response, typically accompanied by a reduction in the peak absorption cross-section<sup>[2]</sup>.

Given our objective, to maximize photothermal conversion while balancing absorption efficiency, these limits represent a reasonable and physically motivated design range. It is worth noting, however, that slight deviations from these assumptions are unlikely to produce significant changes in the overall conclusions.

Once the approximate design limits for the underlying structure (i.e., the traditional core–shell nanoparticle) have been established, we proceed to perform a systematic study based on Mie theory for a double-layered stratified sphere, commonly referred to as a Core–Double–Shell (CDS) nanoparticle. In this analysis, we consider configurations where the core radius,  $r_c$ , ranges from 10 to 75 nm, and the gold shell thickness,  $\delta_{Au}$ , spans from 5 to 15 nm. Regarding the overshell, its thickness,  $\delta_p$ , is varied between 0 and 100 nm. This parameter space is designed to explore the combined influence of geometric and material features on the optical and thermal behaviour of the CSS structures, while remaining within the practical bounds previously identified.

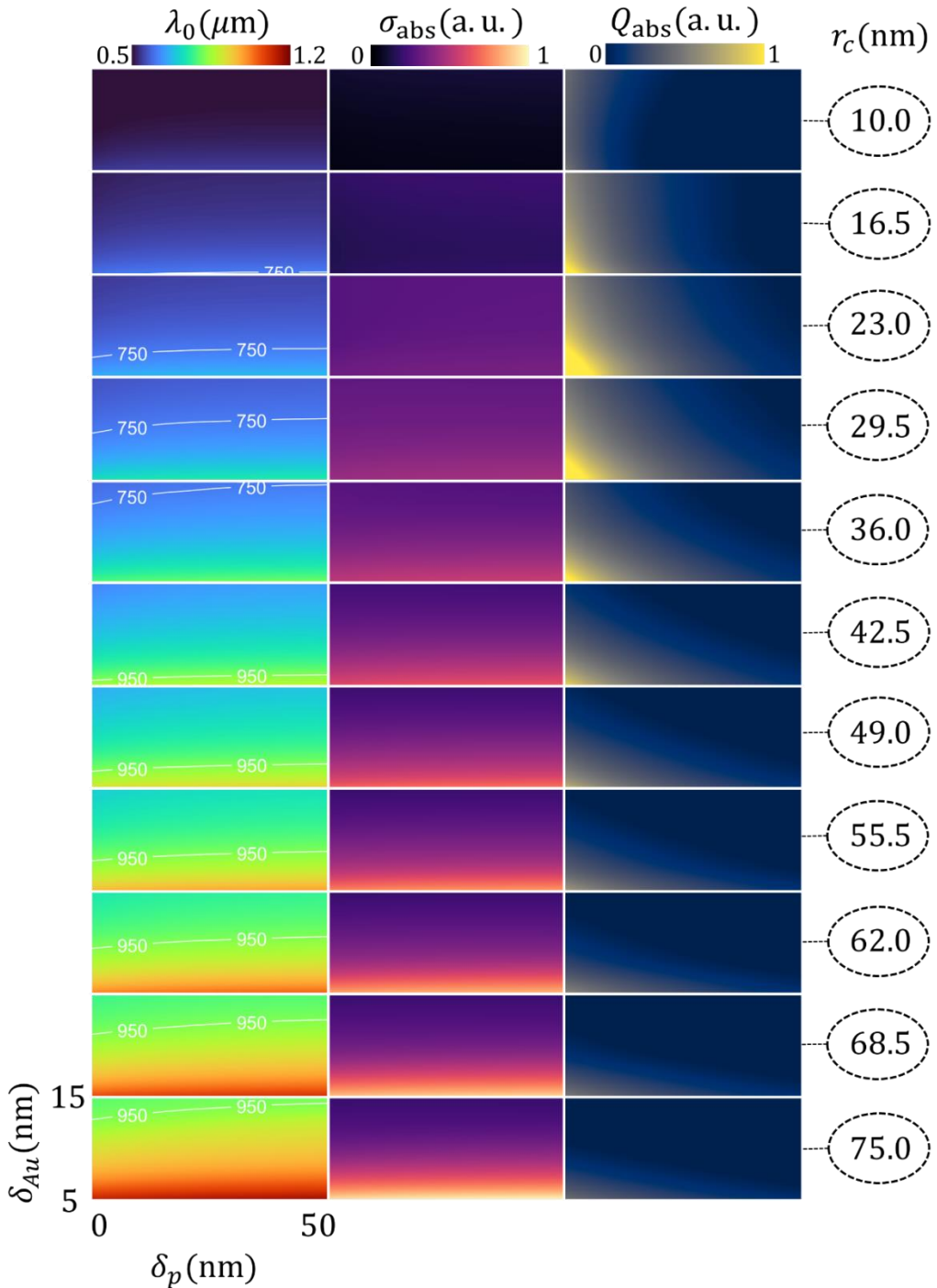


Figure S2. Colour maps showing the spectral and absorption characteristics of core–shell nanoparticles as a function of the gold shell thickness  $\delta_{Au}$  and the polymer coating thickness  $\delta_p$ , for a series of core radii ( $r_c$ ) indicated on the right-hand side. Each row corresponds to a specific core radius, increasing from top to bottom. The three columns respectively represent: (left) the resonance peak wavelength  $\lambda_0$  in micrometers, (centre) the normalized absorption cross-section in arbitrary units  $\bar{\sigma}_{abs}$ , and (right) the absorption efficiency  $\bar{Q}_{abs}$ , also normalized. White contour lines overlaid on the  $\lambda_0$  maps indicate the iso-wavelength levels at 750 nm and 950 nm, which serve as references for identifying plasmonic regimes of interest in the visible and near-infrared ranges.

Figure S2 provides a detailed visualization of the optical response of core–shell–shell (CSS) nanoparticles, considering variations in the core radius, gold shell thickness, and polymer coating thickness. Due to the very limited variation observed at high polymer thicknesses, only the region corresponding to  $\delta_p \in [0, 50]$  nm is shown. Including larger values of the polymer shell would unnecessarily reduce contrast across the maps without offering significant additional insight, as the qualitative behaviour of the system remains essentially unchanged.

Each row corresponds to a fixed value of  $r_c$ , increasing from top to bottom from 10 to 75 nm, while each column represents a different quantity of interest: the resonance peak wavelength  $\lambda_0$  (left), the normalized absorption cross-section  $\bar{\sigma}_{abs}$  (centre), and the absorption efficiency  $\bar{Q}_{abs}$  (right). The data shown are the result of rigorous calculations based on Mie theory for multi-layered spheres<sup>[3]</sup>.

A clear and progressive redshift of the plasmonic resonance is observed as the core radius increases. For small cores ( $r_c \approx 10$  nm), the resonance remains in the visible range, far from the biologically relevant near-infrared window. As core radius increases, the peak wavelength shifts toward longer values, entering the first biological transparency window (roughly 750–950 nm). This trend is particularly notable for  $r_c \geq 36$  nm, where the resonance remains confined within this spectral region for a broad range of gold and polymer thicknesses. The white contour lines overlaid on the  $\lambda_0$  maps, at 750 nm and 950 nm, serve as visual guides to identify the configurations falling within this therapeutically relevant window.

The behaviour of the normalized absorption cross-section reveals that the overall strength of absorption increases with both core size and gold shell thickness. However, the dependence on the polymer layer is comparatively weak, as anticipated, with only a modest modulation of the absorption strength across the explored range.

In terms of absorption efficiency, which accounts for the geometrical size of the nanoparticle, the results point to a more complex scenario. Although the absolute absorption increases with particle size, the efficiency is highest for intermediate-sized particles, typically in the range of  $r_c \approx 23 – 36$  nm, especially when combined with a gold shell of thinner thickness (around 5–10 nm). This behaviour reflects the competing roles of resonant absorption enhancement and geometrical reduction: large particles collect more energy in absolute terms but distribute it over a proportionally larger surface, reducing their relative efficiency. Conversely, very small particles exhibit high efficiency but weak absolute absorption and poorly positioned resonances.

Taken together, Figure S2 illustrates a coherent physical picture: intermediate-sized core–shell–shell nanoparticles with thin gold layers and moderate polymer coatings are optimal for achieving resonances within the first biological window while simultaneously maximizing expected directional photothermal efficiency. These findings provide a rational basis for narrowing the design space in subsequent stages, allowing for targeted optimization of structures intended for biomedical applications such as selective heating or photothermal therapy. However, a method or procedure is needed to rationally select the best candidate.

With these data, the goal is to maximize both absorption and efficiency to generate as much temperature as possible. While maximizing absorption is compatible with increasing the thickness of the polymer coating, simply by moving toward larger structures, another key objective of this work is to achieve efficient thermal directionality. Previous studies<sup>[4-6]</sup> have shown that the ability to direct heat depends on the presence of an insulating layer within the structure. Therefore, designs with significantly thick polymer layers will be explored. The simultaneous maximization of these three parameters imposes a trade-off between maximum absorbed energy and directional control, as increasing the polymer thickness reduces the particle’s absorption efficiency. To determine the optimal structure based on a balanced maximization of these three parameters, the following trade-off function is defined:

$$\mathcal{F} = \bar{\sigma}_{abs}^{\gamma_1} \bar{Q}_{abs}^{\gamma_2} \bar{\delta}_p^{\gamma_3} \quad (S1)$$

where  $\gamma_1, \gamma_2, \gamma_3 \in [1, 1.5]$  and

$$\bar{\sigma}_{abs} = \frac{\sigma_{abs}}{\max\{\sigma_{abs}\}} \quad (S2)$$

$$\bar{Q}_{abs} = \frac{Q_{abs}}{\max\{Q_{abs}\}} \quad (S3)$$

$$\bar{\delta}_p = \left( \frac{\delta_p}{r_c + \delta_{Au} + \delta_p} \right)^2 \quad (S4)$$

All variables have been normalized so that their contribution to the trade-off function is dimensionless and as balanced as possible, given the contrasting nature of their absolute magnitudes ( $\sigma_{abs} \ll Q_{abs} < \delta_p$ ). In all cases, the maxima of the absorption cross section and the absorption efficiency have been computed as the global maxima across the entire dataset. In this way, the trade-off function  $\mathcal{F}$  is calculated considering all the exponents are equal to 1. The maximization process consisted in obtaining a two-dimensional data set for each  $r_c$  containing the values for  $\mathcal{F}$  as a function of  $\delta_p$  and  $\delta_{Au}$ . Then the maximum value is stored for each  $r_c$ . Finally, the global maximum is obtained from a last maximization.

This information is shown in Figure S3. It can be observed that the compromise function yields a maximum for intermediate-sized structures, as expected. This behaviour arises because, in general, achieving higher absorption requires larger particles with minimal gold shell thicknesses, while the effect of the polymer layer remains marginal. However, when maximizing efficiency, larger structures are penalized, leaving intermediate-sized configurations as the most suitable candidates for reasonably thick polymer coatings. Therefore, for this particular set of exponents, the most appropriate configuration is:  $(r_c, \delta_{Au}, \delta_p) = (36, 5, 21)$  nm.

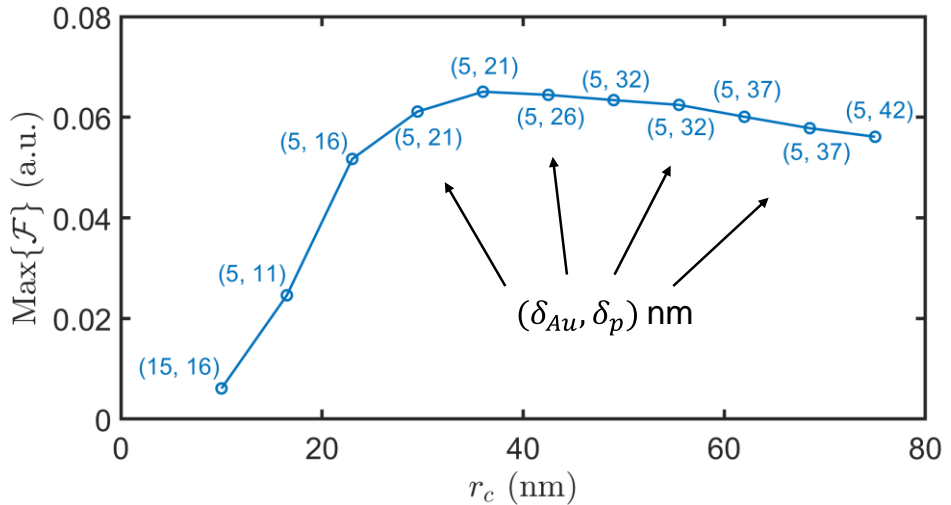


Figure S3. Local maxima of the trade-off function  $\mathcal{F}$  for each core radius. Each ordered pair represent a vector with the corresponding gold ( $\delta_{Au}$ ) and polymer ( $\delta_p$ ) thicknesses respectively.

Besides, as shown in Figure S3, the trade-off function varies slowly for larger structures. This suggests that the influence of the different parameters may not be homogeneous. Although all quantities lie within the same order of magnitude, their dependence on the gold and polymer layer thicknesses can lead to uneven contributions, potentially masking the effect of one parameter over another. To mitigate this, three exponent values,  $\gamma_1$ ,  $\gamma_2$  and  $\gamma_3$  are considered. The range of exponent values, from 1 to 1.5, has been deliberately chosen to prevent combinations that would cause one parameter to dominate the others, effectively reducing the compromise function to the maximization of a single quantity. By restricting the exponents to this moderate range, we ensure that all parameters contribute comparably, preserving the integrity of the trade-off function optimization.

The trade-off function is then computed over the entire dataset for every possible combination of exponents. In this way, for each triplet of exponents, the configuration that globally

maximizes the trade-off function is identified. This approach not only yields a single global maximum but captures all possible global maxima associated with the different exponent sets. As a result, the selection of the optimal structure is reduced to a frequency-based analysis (Figure 1b in the main text), identifying a feasible range of structural parameters. This is consistent with the decision-making process required, since, given the passive nature of thermal transport processes, it is reasonable to expect that no single polymer thickness will be universally optimal.

## II. Conductive thermal flux characterization.

One of the main objectives of this manuscript is not only to quantify the amount of thermal energy delivered to each half-space, but also to assess the degree of directionality or focusing of that energy as a function of the configuration. To characterize the degree of directionality in COMSOL, the conductive heat flux is integrated over a spherical surface, concentric with the nanoparticle under analysis. Using this same surface, the same quantity is iteratively integrated over a spherical cap defined by a solid angle  $\Omega$ , which subtends a semi-aperture angle  $\alpha$  such that:

$$\Omega(\alpha) = 2\pi R^2(1 - \cos(\alpha)) \quad (S5)$$

By dividing the heat flux crossing the spherical cap by the total flux over the full spherical surface, one obtains the fraction of thermal energy generated by the particle that is emitted into a given region of space. This quantity provides a direct measure of the degree of thermal directionality. As shown in Equation X, this procedure yields a value for each chosen semi-aperture angle  $\alpha$ . Accordingly, we define the *directionality angles* as the set  $\{\alpha_i\}_{i \in I}$  such that the fraction of energy crossing the corresponding spherical caps  $\{\Omega_i\}_{i \in I}$ , are  $\{\eta_i\}_{i \in I}$  respectively. To validate and illustrate the suitability of this approach, we perform the analysis in the paradigmatic case of a gold nanosphere embedded in a homogeneous aqueous environment under continuous illumination. In this scenario, the heat flux is expected to be purely radial and isotropic<sup>[7]</sup>, so that in spherical coordinates the vector field can be written as:  $\vec{\Phi}(r, \theta, \phi) = (\Phi(r), 0, 0)$ . Given that the outward normal to the spherical integration surface is  $\vec{n} = \vec{e}_r$ , in this coordinate system, it follows that:

$$\eta(\alpha) = \frac{\iint_{\Omega(\alpha)} \vec{\Phi} \cdot \vec{n} \, dS}{\iint_{S^2} \vec{\Phi} \cdot \vec{n} \, dS} = \frac{1}{2}(1 - \cos(\alpha)) \quad (S6)$$

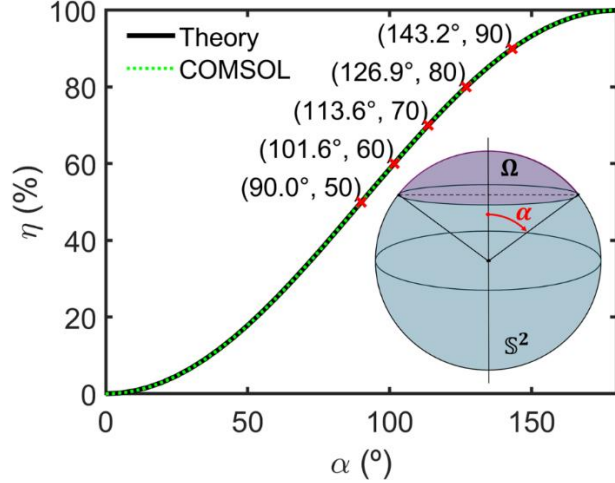


Figure S4. Power fraction  $\eta(\alpha)$  crossing a spherical cap of semi-aperture angle  $\alpha$ , computed for a homogeneous gold sphere in water under continuous illumination. The analytical prediction (black curve) is in excellent agreement with COMSOL simulations (green dashed line). Red crosses indicate specific threshold values, with each pair  $(\alpha, \eta)$  marked on the curve. Notably, an aperture angle of  $90^\circ$  encloses exactly 50% of the emitted power, while capturing 90% of the thermal energy requires  $\alpha \approx 143^\circ$ . The inset illustrates the integration geometry, where  $\Omega$  denotes the cap subtended by  $\alpha$  over the spherical surface  $\mathbb{S}^2$ .

Figure S4 shows the fraction of thermal power crossing a spherical cap as a function of the semi-aperture angle defining the cap, in the case of a homogeneous gold sphere. It can be observed that for an angle of  $90^\circ$ , which corresponds to the entire upper half-space, the particle delivers exactly 50% of the generated energy. To enclose 90% of the total thermal power, the aperture must be extended beyond  $140^\circ$ . This result highlights the absence of directionality in this reference structure. When combined with the temperature map, this analysis provides an excellent baseline for comparing the directional behaviour and degree of thermal focusing in more complex architectures. Since we are interested in the directionality towards the upper hemisphere, the value  $\eta = 50\%$  will be typically taken as a reference since in the symmetric case corresponds to the half of the total generated power.

### III. Energy density intensification and gain parameter definition.

#### a) Physical motivation.

The asymmetric structures under consideration redirect part of the thermal flux toward the upper hemisphere, thereby concentrating the emitted energy over a smaller spherical surface compared to a symmetric configuration. To quantify the resulting local intensification of surface energy density, we define a relative gain parameter  $G$  that, for each energy level  $\eta$ ,

compares the spherical area covered by that fraction of energy in the studied structure to that of the symmetric case.

b) Definition of  $G$ .

As seen in Figure S4, the generated energy fraction is defined as the amount of energy per unit time (i.e., power) that passes through a spherical surface subtended by a solid angle  $\Omega(\beta)$ , normalized by the total power emitted by the structure. This quantity captures how much of the emitted energy is directionally distributed within a given angular region and serves as a basis for evaluating thermal redirection and focusing effects.

$$\eta(\beta) = \frac{\iint_{\Omega(\beta)} \vec{\Phi} \cdot \vec{n} \, dS}{\iint_{S^2} \vec{\Phi} \cdot \vec{n} \, dS} = \frac{P(\beta)}{P_T}$$

In this way, for each energy fraction, one can associate a spherical surface area defined by the solid angle  $\Omega(\beta)$ , which in turn allows that energy level to be identified with a corresponding semi-angle  $\beta$  in a well-defined mathematical manner. The area of this spherical surface is expressed as:

$$A(\beta) = 2\pi R^2(1 - \cos(\beta)) \quad (S7)$$

where  $R$  is the radius of the control sphere surface through which the energy flux is evaluated. This expression for the area can be further particularized within our context. Specifically, the area of the spherical surface subtended by the energy fraction  $\eta$  for a structure with an aperture angle  $\theta$  is given by:

$$A(\eta, \theta) = 2\pi R^2(1 - \cos(\beta_\theta(\eta))) \quad (S8)$$

Thus, for a fixed energy fraction  $\eta$ , the power density crossing the spherical control surface can be computed as:

$$I(\eta, \theta) = \frac{\eta \cdot P_{tot}}{A(\eta, \theta)} = \frac{\eta \cdot P_{tot}}{2\pi R^2(1 - \cos(\beta_\theta(\eta)))} \quad (S9)$$

where  $P_{tot}$  is the total power generated by the structure. This expression quantifies how concentrated the emitted energy is on the spherical surface, serving as the basis for defining the relative gain. Given a fixed value of  $\eta$ , there exists a corresponding angle  $\beta$  that defines the spherical cap enclosing that energy level. To assess how the energy density on the control surface becomes enhanced, we compute the angle  $\beta_0(\eta)$  that defines the spherical cap required to enclose the same energy fraction  $\eta$  in the **symmetric case** ( $\theta = 0^\circ$ ). The associated area is denoted as  $A(\eta, 0)$ . Accordingly, the power density in the symmetric case can be expressed as:

$$I(\eta, 0) = \frac{\eta \cdot P_{tot}}{A(\eta, 0)} = \frac{\eta \cdot P_{tot}}{2\pi R^2(1 - \cos(\beta_0(\eta)))} \quad (S10)$$

It is worth noting that, since the objective is to assess the **energy density**, the absolute magnitude of the total emitted power is not of primary importance. For this reason, we assume a symmetric reference case that emits the same total power as the asymmetric structure, within the same spatial domain. Under this assumption, the **gain** is defined by comparing the power density of the asymmetric configuration with that of the symmetric case, leading to:

$$G(\eta, \theta) = \left( \frac{I(\eta, \theta)}{I(\eta, 0)} - 1 \right) \cdot 100 = \left( \frac{1 - \cos(\beta_0(\eta))}{1 - \cos(\beta_\theta(\eta))} - 1 \right) \cdot 100 [\%] \quad (S11)$$

which expresses the relative enhancement of energy density induced by the asymmetry, at a given energy level  $\eta$  for the aperture angle  $\theta$ , in percentage terms. Since any degree of structural asymmetry induces thermal asymmetry, the ratio  $I(\eta, \theta)/I(\eta, 0)$  is always greater than 1. Therefore, in order for the gain  $G(\eta, \theta)$  to represent a **percentage increase** in energy density, the unit value is subtracted from the ratio. This allows for a direct and visual interpretation of the gain as:

- $G > 0$ : the same energy fraction  $\eta$  is confined within a smaller spherical cap, thereby increasing the energy density crossing the surface.
- $G = 0$ : no intensification occurs, which corresponds to a fully symmetric case.
- The larger the value of  $G$ , the stronger the thermal focusing effect.

### c) Physical interpretation of the gain metric

A particularly illustrative case is that of  $\eta = 0.5$ , which corresponds to the fraction of energy directed into the upper hemisphere ( $\beta = 90^\circ$ ) in a fully symmetric configuration ( $\theta = 0^\circ$ ). In such a symmetric case, the energy is uniformly emitted in all directions, so precisely half of the total energy flows through the upper half-space. This sets a reference angular threshold:  $\beta_0(0.5) = 90^\circ$ , and the corresponding area is that of a hemisphere.

When structural asymmetry is introduced, the same energy fraction  $\eta = 0.5$  becomes concentrated into a smaller solid angle, i.e., a cap of radius  $\beta_\theta(0.5) < 90^\circ$ . This angular compression implies that the same amount of energy crosses a reduced surface, increasing the local energy density. The relative gain  $G(\eta, \theta)$  thus quantifies this enhancement.

For instance, if a given structure yields  $G = 30\%$  at  $\eta = 0.5$ , this means that the half of the total emitted energy is now confined within a surface whose area is 30% smaller than that of the hemisphere. From the gain expression:

$$G(\eta, \theta) = \left( \frac{1 - \cos(\beta_\theta(\eta))}{1 - \cos(\beta_0(\eta))} - 1 \right) \cdot 100 \quad (S12)$$

and knowing that  $\cos(\beta_0) = \cos(90^\circ) = 0$ , we find that  $1 - \cos(\beta_\theta) = 0.7$ , so  $\cos(\beta_\theta) = 0.3$ , which gives  $\beta_\theta \approx 72.5^\circ$ . In this case, 50% of the energy is emitted within a cone of only  $72.5^\circ$ , compared to  $90^\circ$  in the symmetric case.

For a stronger effect, say  $G = 50\%$ , we have  $1 - \cos(\beta_\theta) = 0.5$ , so  $\cos(\beta_\theta) = 0.5$ , yielding  $\beta_\theta = 60^\circ$ . This indicates that the same amount of energy is now emitted within just one quarter of the spherical surface, a strong indication of directional thermal emission.

This metric thus offers a direct and quantitative way to evaluate how effectively a structure redirects and concentrates thermal energy, providing insight into both the angular confinement and surface densification induced by asymmetry.

#### IV.-Calculation of the relaxation time.

The pulse duration under investigation is defined based on the computed transient thermal response. The system's peak temperature is subsequently fitted using the following model<sup>[7]</sup>:

$$m(t) = A \left( 1 - \text{erf} \left( \frac{B}{\sqrt{t}} \right) \right) \quad (S13)$$

where  $A = T_\infty$  is a fitting constant associated with the steady-state temperature, while  $B^2 = R/4D_s$  represents the squared fitting constant corresponding to the characteristic heating time. According to this expression, the parameter  $B^2$  can be interpreted as the time at which the temperature reaches approximately 16% of the stationary value. However, in this work, the relevant timescale is taken as the time required to reach 84% of the stationary temperature. This matches the asymptotic growth properties of the error function.

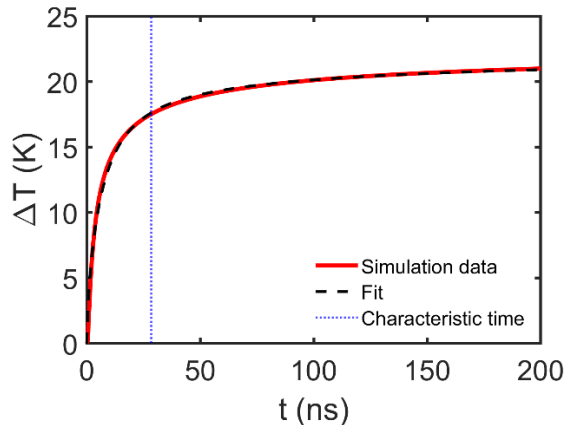


Figure S5. Temperature rise of a CSS defined by  $(r_c, \delta_{Au}, \delta_p, \theta) = (36 \text{ nm}, 5 \text{ nm}, 40 \text{ nm}, 70^\circ)$ . The red and the black dashed lines correspond to the simulated and fitted temperatures. The blue vertical line stands for the time for which the structure reaches an 84% of the stationary temperature.

The fitting is shown in Figure S5. It can be seen that the model fits very well the simulated data. The relative fitting error  $\sigma$  is calculated as the mean of the sum of squared residuals over the stationary temperature:  $\sigma \approx 0.2\%$ . Based on this fitting, a characteristic heating time of approximately 30 ns is obtained under the present conditions.

## References

- [1] P. K. Jain, "Gold Nanoparticles for Physics, Chemistry, and Biology. Edited by Catherine Louis and Olivier Pluchery.,," *Angewandte Chemie International Edition* **53**(5), 1197 (2014).
- [2] J. González-Colsa, G. Serrera, J. M. Saiz, D. Ortiz, F. González, F. Bresme, F. Moreno, P. Albella, *Opt Express* **2022**, *30*, 125.
- [3] J. Schäfer, MatScat (<https://www.mathworks.com/matlabcentral/fileexchange/36831-matscat>), *MATLAB Central File Exchange* **2025**.
- [4] J. D. Olarte-Plata, J. Gabriel, P. Albella, F. Bresme, *ACS Nano* **2022**, *16*, 694.
- [5] J. González-Colsa, A. Franco, F. Bresme, F. Moreno, P. Albella, *Sci Rep* **2022**, *12*, 14222.
- [6] J. González-Colsa, F. Bresme, P. Albella, *The Journal of Physical Chemistry C* **2023**, *127*, 19152.
- [7] G. Baffou, *Thermoplasmonics*, Cambridge University, **2018**.